An optimized rapid analytical workflow for applying magnetite as an indicator mineral for porphyry copper deposits

Rebecca Morris[1, a], Dante Canil[1], and Terri Lacourse[2]

[1] School of Earth and Ocean Sciences, University of Victoria, Victoria, BC, V8W 3P6
[2] Department of Biology, University of Victoria, Victoria, BC, V8W 3P6
[a] corresponding author: ramorri@uvic.ca

Recommended citation: Morris, R., Canil, D., and Lacourse, T., 2025. An optimized rapid analytical workflow for applying magnetite as an indicator mineral for porphyry copper deposits. In: Geological Fieldwork 2024, British Columbia Ministry of Mining and Critical Minerals, British Columbia Geological Survey Paper 2025-01, pp. 93-103.

Abstract

The discrimination of hydrothermal magnetite in till samples near the Mount Polley porphyry copper deposit was re-examined using revised methods that optimized the analytical workflow by laser ablation inductively coupled mass spectrometry (LA-ICP-MS). We show that decreasing laser ablation dwell times to as little as 10 seconds with 100 µm ablation spot sizes results in nearly identical scores for the percentages of hydrothermal magnetite in bulk till samples compared to more time-consuming methods that use longer dwell times and data reduction to edit possible inclusions. The reproducibility in the identification of hydrothermal magnetite from linear discriminant analysis (LDA) models of Pisiak et al. (2017) indicates their LDA2 model, which includes Ti, is better than LDA1, where scoring results of hydrothermal magnetite from the revised methods are within 6%. Reproducibility in identifying hydrothermal magnetite with the commonly used Ti versus Ni/Cr discriminant space is generally poor (<40%). Our work highlights that basaltic glass calibration standards are better than NIST glass calibration standards for analyzing magnetite because the latter have Fe contents far below (ppm concentrations) that of magnetite (up to 72 wt.% Fe). Future work could further optimize workflow by including a calibration standard closer to magnetite in matrix composition.

Keywords: Porphyry copper deposits, magnetite, indicator minerals, laser ablation inductively coupled mass spectrometry, optimized workflow exploration

1. Introduction

Porphyry copper deposits are an important source of critical metals such as copper, which are required for Canada's transition to a net-zero emissions economy (NRCan, 2022). With seven active porphyry mines in British Columbia (Red Chris, Mount Milligan, Copper Mountain, Gibraltar, Highland Valley Copper, Mount Polley, and New Afton), the province is the top producer of copper and only producer of molybdenum in Canada (Clarke et al., 2024). These mines are in some of the largest and best-exposed deposits in the province. Future discovery and development of buried porphyry copper deposits will benefit from exploration using minerals in sediments as indicators. Weather-resistant minerals, such as magnetite, could be used to assist in locating porphyry copper deposits buried beneath glacial drift in the Canadian Cordillera (Pisiak et al., 2017), or from stream sediments (McCurdy et al., 2022). Magnetite is an ideal indicator mineral for this purpose because it is physically resistant and its chemistry varies with its formation conditions over a broad range of temperatures, pressures, bulk compositions, and oxygen fugacity, in both igneous and hydrothermal environments (Nadoll et al., 2014).

Numerous studies have investigated the geochemical variability in magnetite to discriminate between processes of formation, such as crystallization from a silicate melt (herein 'igneous magnetite') or precipitation from a hydrothermal fluid (herein 'hydrothermal magnetite') (Dupuis and Beaudoin, 2011; Nadoll et al., 2014; Canil et al., 2016; Pisiak et al., 2017; Wen et al., 2017; Sievwright, 2018; McCurdy et al., 2022). Hydrothermal magnetite has been used in exploration to target mineralization such as in porphyry copper deposits. Recent work (Pisiak et al., 2017; Wen et al., 2017) has shown that many commonly used bivariate discriminant diagrams to identify hydrothermal magnetite (Dupuis and Beaudoin, 2011; Nadoll et al., 2015) are ineffective. To improve matters, Pisiak et al. (2017) performed linear discriminant analyses which applies multivariate statistical methods on numerous trace elements in magnetite (Mg, Al, V, Mn, Co, Ni ±Ti; all normalized to Fe) to make a more robust discrimination of hydrothermal magnetite.

In this study, we employ the linear discriminant analyses methods of Pisiak et al. (2017) but optimize the analytical workflow in an effort to make the identification of ore-related hydrothermal magnetite in till and stream samples more rapid, simple, and efficient. To do this, we re-analyzed magnetite by LA-ICP-MS in subglacial till samples collected surrounding the Mount Polley porphyry copper deposit (Pisiak et al., 2017). We examined the reproducibility in scoring of hydrothermal magnetite in these samples with adjustments to workflow such as automating the LA-ICP-MS system, reducing laser

dwell times, and varying ablation parameters (spots versus raster lines, increased spot size to 100 µm), and using different calibration standards.

2. Geological setting

The Mount Polley porphyry copper deposit (MINFILE 093A 008) is in the Quesnel terrane, south-central Canadian Cordillera (Fig. 1; Logan and Mihalynuk, 2005; Logan et al., 2007) within Secwepemcúl'ecw. The deposit is in late Triassic monzonite and diorite intrusions of the Mount Polley intrusive complex (Fig. 2) that were emplaced into Triassic Nicola Group volcanic rocks (Logan and Mihalynuk, 2005; Logan et al., 2007). Hydrothermal breccias with potassic-sodic to calc-potassic alteration and hydrothermal magnetite are spatially associated with mineralization, typically near or along faults (Logan and Mihalynuk, 2005; Rees, 2014). The age of mineralization is 205.2 ±1.2 Ma, determined by $^{40}Ar/^{39}Ar$ of hydrothermal biotite intergrown with chalcopyrite (Logan et al., 2007). Unmineralized volcanic rocks that overlie the mineralization have been dated at 196.7 ±1.3 Ma (U-Pb zircon; Logan et al., 2007).

Tills from the late Wisconsin Fraser Glaciation (~29-12 ka; Ryder et al., 1991) were deposited on much of the Quesnel terrane, including the area surrounding the Mount Polley deposit. Ice-flow indicators show early westward (oriented 250-275°) and late northwestward (oriented 290-330°) movements (Fig. 2; Hashmi et al., 2015).

3. Methods

Approximately 50 magnetite grains (0.25-2 mm in size) from each of three subglacial till samples previously analyzed by Pisiak et al. (2017; 12-PMA-094-A01, 12-PMA-098-A01, and 12-PMA-101-A02) were re-analyzed for major and trace element concentrations by LA-ICP-MS at the University of Victoria. The complete set of analytical results are provided in a supplementary data file (Morris et al., 2025).

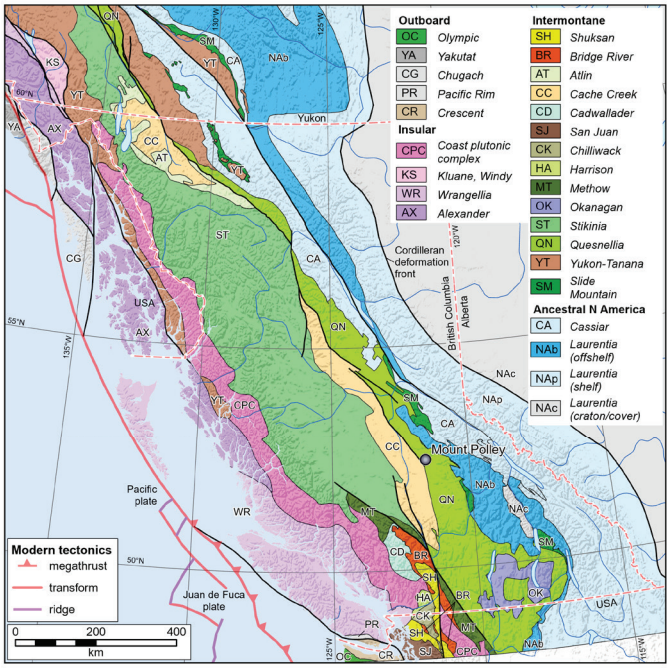

Fig. 1. Location of Mount Polley deposit. Terranes after Colpron (2020).

For this study, we used an Agilent 8800 triple quadrupole (Q3) inductively coupled plasma mass spectrometer (ICP-MS) coupled to a Teledyne CETAC LSX-213 G2+ with an argon gas carrier system, which differs from the Thermo Scientific XSERIES double quadrupole (Q2) ICP-MS coupled to a New Wave UP-213 used by Pisiak et al. (2017). Laser settings for this study were as follows: laser output=30%, fluence 6.12 J/m^2, laser frequency=10 Hz, signal acquisition time=10-40 seconds, baseline acquisition time=30 seconds, spot size=100 µm. Optimal laser settings are unique to different lasers, conditions, and phases analyzed, thus need to be adjusted accordingly. We employed automation mode between the laser and ICP-MS. Automation mode allows the user to pre-select ablation locations (~2-3 minutes per location) and run analyses without supervision, saving the user monitoring time. Because uncertainty on automatic stage movement between samples is within 20 µm, ablation spots were pre-selected >20 µm from grain edges, obvious inclusions, and previously ablated regions. Standards (calibration and external) were analyzed at the start and end of analyses and every 10-15 magnetite grains.

Samples are from subglacial till collected by Plouffe and Ferbey (2016) near the Mount Polley deposit (Fig. 2). Three of those samples with notable proportions (~16-22%) of magnetite previously identified as hydrothermal by Pisiak et al. (2017) were selected for this study. Till samples directly overlying the Mount Polley intrusive suite were not selected because they previously recorded <15% hydrothermal grains (Pisiak et al., 2017). Major, minor, and trace elements measured in magnetite included: ^{57}Fe, ^{47}Ti, ^{25}Mg, ^{27}Al, ^{51}V, ^{52}Cr, ^{55}Mn, ^{59}Co, ^{60}Ni, ^{63}Cu, and ^{66}Zn. In addition, ^{23}Na, ^{29}Si, ^{31}P, ^{34}S, ^{39}K, ^{42}Ca, and ^{137}Ba were analyzed to detect inclusions (e.g., apatite) and for sum normalization used in data reduction methods for magnetite samples and standard reference materials. Similar to Pisiak et al. (2017), the sum normalization method of Liu et al. (2008); Ablation Correction Yield Factor method) was used, which allows for calibration independent of an internal standard. Pisiak et al. (2017) showed how sum normalization is advantageous to internal standards that use electron microprobe analysis of major element concentrations in magnetite, because of the focused beam size (<5 µm) and common heterogeneity present in exsolved and altered magnetite (e.g., titanomagnetite-ilmenite exsolution in igneous magnetite; replacement of hydrothermal magnetite by titanite or hematite). This heterogeneity is documented petrographically in many types of magnetite (Haggerty, 1976, 1991; Pisiak et al., 2017; Wen et al., 2017; Huang et al., 2019; Xiao et al., 2023).

Data reduction and calibration were completed at the University of Victoria using the Iolite™ (v4.9.4) software package (Paton et al., 2011; Paul et al., 2023). We employed and

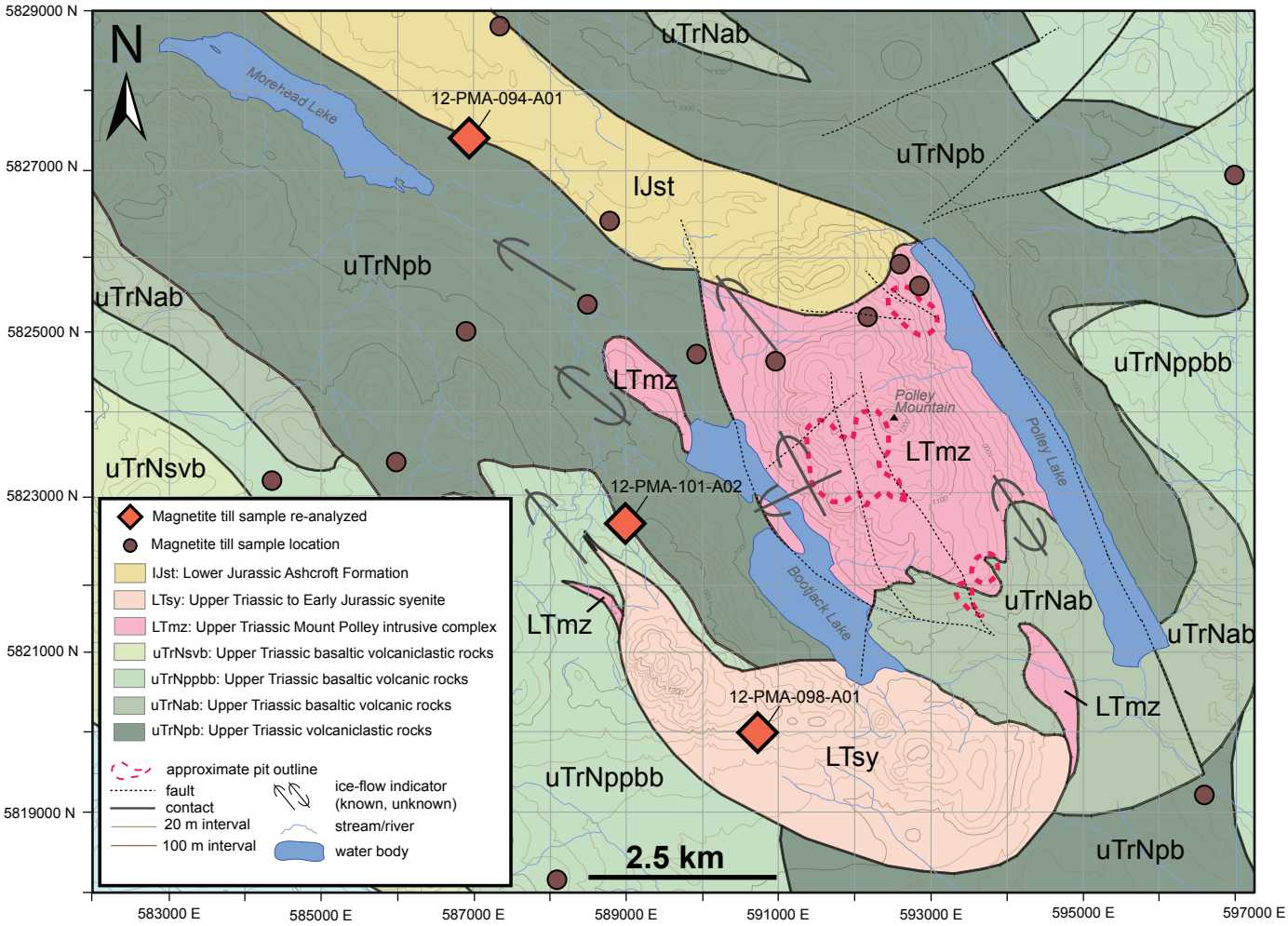

Fig. 2. Subglacial till sample locations from Pisiak et al. (2017) including those re-analyzed in this study. Bedrock geology from Logan et al. (2010), Rees et al. (2014), and Cui et al. (2017), ice-flow indicators from Hashmi et al. (2015). Approximate pit outline from Rees et al. (2014). UTM zone 10U (093A052 quadrangle) using NAD83 projection.

tested various analytical workflows and calibration standards, using four methods. Method 1 was performed by editing time-resolved spectra around obvious inclusions (notably apatite) encountered at depth during laser ablation. This method used BCR-2g and NIST 613 standards for calibration, and NIST 611 as an external standard (Table 1). Method 2 was identical to Method 1 but instead used NIST 611 and NIST 613 standards for calibration, similar to Pisiak et al. (2017). External standards used were BCR-2g and BHVO-2g (Table 1). Method 3 used only the first 10 seconds of ablation data, without consideration of inclusions. This method used BCR-2g and NIST 613 standards for calibration, and BHVO-2g as an external standard (Table 1). Method 4 was performed by collecting the entire 40 seconds of ablation data, without considering inclusions. This method used BCR-2g and NIST 613 standards for calibration, and BHVO-2g as an external standard (Table 1). An optional downhole fractionation correction factor was applied to Method 4 to account for potential fractionation effects over the entire time-resolved spectra (40 seconds).

4. Results

4.1. Data accuracy and precision

To quantify data quality, we assess accuracy using the relative per cent differences between known and measured values on external standards (Table 1) and evaluate precision through the relative standard deviations from repeat analyses of these standards (Morris et al., 2025). External standards vary between methods and samples analyzed (Table 1). For sample 12-PMA-094-A01, NIST 611 was used as an external standard for Methods 1, 3, and 4 (Table 1). However, due to higher relative per cent differences between known and measured values for some NIST 611 elements (>10% Mg, Ti, P, S, Cu, Zn; Table 1), we switched to BHVO-2g as an external standard for Methods 1, 3, and 4 for remaining sample analyses (12-PMA-098-A01 and 12-PMA-101-A02; Table 1). Relative per cent differences between known and measured values, for BHVO-2g were <10% for all elements for samples 12-PMA-098-A01 and 12-PMA-101-A02 (Methods 1, 3, and 4), with

Table 1. External reference material relative per cent differences between known and measured values for various methods.

		External Standard RPD		
Sample ID	**Method**	**NIST 611**	**BHVO-2g**	**BCR-2g**
12-PMA-094-A01	1	<10% (S -13%; Cu -11%)	n/a	calibrant
	2	calibrant	n/a	<10% (Cr -10%; Cu -22%; Zn +16%)
	3	<10% (Mg, P +11%; S -13%; Ti +14%; Cu -10%)	n/a	calibrant
	4	<10% (Mg, P, Ti +11%; S -14%; Zn -10%)	n/a	calibrant
12-PMA-098-A01	1	n/a	all elements <10%	calibrant
	2	calibrant	<10% (Fe -18%; Ni +11%; Zn +20%)	<10% (Mn -11%; Fe -18%; Cu -18%; Zn +26%)
	3	n/a	all elements <10%	calibrant
	4	n/a	all elements <10%	calibrant
12-PMA-101-A02	1	n/a	<10% (Cu -11%)	calibrant
	2	calibrant	<10% (V +14%; Fe -14%; Co +20%; Zn +10%)	<10% (Ti -11%; Fe -13%; Co +15%; Cu -19%; Zn +18%)
	3	n/a	<10% (Cu -11%)	calibrant
	4	n/a	<10% (Cu -11%)	calibrant

RPD is relative % difference of measured versus known (preferred) values for elements where <10% (Fe -18%; Ni +11%; Zn +20%) refers to <10% RPD for all elements, except for Fe, Ni, and Zn (corresponding RPDs shown). RPD calculated as follows: $(known_i - measured_i)/(known_i + measured_i)*100$; where $known_i$ refers to the known and preferred reference value of an element in an external standard, and $measured_i$ is the measured concentration (mean of replicate external standard analyses) of that element.

the exception of Cu (-11%) for sample 12-PMA-101-A02 (Table 1). For Method 2, we used BHVO-2g and/or BCR-2g as external standards, because neither were used as calibration standards in this method (Table 1). Method 2, which uses NIST glasses (611, 613) as calibration standards, reported the greatest relative per cent differences between known and measured values for certain elements (>10% ±Fe, Ti, Ni, V, Cr, Mn, Cu, Zn, Co) (Table 1). Known values for external and calibration standards were obtained from Jochum et al. (2011; NIST 611, 613) and Jochum et al. (2005; BHVO-2g and BCR-2g). Relative standard deviations calculated from repeat analyses of external standards were within 10% for all elements, regardless of the external standard used and method, with the exception of S for samples 12-PMA-094-A01 (Method 2) and 12-PMA-098-A01 (all methods; Morris et al., 2025).

Element concentrations from the sum normalization method of Liu et al. (2008) were compared to concentrations obtained using Si as an internal standard for external standards NIST 611, BCR-2g, and BHVO-2g with known and preferred Si values (Jochum et al., 2005; Jochum et al., 2011). Comparisons between mean element concentrations of external standards from sum normalization versus using an internal standard were

within 3% (Morris et al., 2025). Because ablations were made on new locations of the same magnetite grains and our adjusted sum normalization techniques included additional elements (Na, P, S, K, Ba), we do not compare mean trace element concentrations of our results on magnetite grains with those of Pisiak et al. (2017). However, comparison of Fe concentrations from each of our methods to those of Pisiak et al. (2017) is within 10%, except for one magnetite grain (D8) in sample 12-PMA-098-A01, and only for Method 3 (Fe, relative per cent difference=12%). Nonetheless, we expect some variation in Fe content within grains, given the heterogeneity in magnetite and the potential for ilmenite-titanomagnetite exsolution (Haggerty, 1976, 1991; Pisiak et al., 2017; Wen et al., 2017; Huang et al., 2019; Xiao et al., 2023).

4.2. Hydrothermal magnetite scoring from linear discriminant analyses

Given that the purpose of this work is to complete a comparative study to Pisiak et al. (2017), we use their linear discriminant analyses to identify hydrothermal magnetite in till samples 12-PMA-094-A01, 12-PMA-098-A01, and 12-PMA-101-A02. The linear discriminant analyses (LDA1 and LDA2 models) performed by Pisiak et al. (2017) determined which elements in magnetite have the most discriminating power from known ore-related hydrothermal magnetite, ore igneous magnetite, and barren igneous magnetite to define discriminant functions that uniquely identify a magnetite source (cf. Table 3 in Pisiak et al., 2017). For more details on the linear discriminant analyses statistical methods see Pisiak (2015) and Pisiak et al. (2017). Linear discriminant analysis model formulas and calculations are as follows, and are provided in Pisiak (2015),

For LDA1:

$$F1 = 0.703 * \ln\left(\frac{Mg}{Fe}\right) - 1.387 * \ln\left(\frac{Al}{Fe}\right) - 0.075 * \ln\left(\frac{V}{Fe}\right) + 0.412 * \ln\left(\frac{Mn}{Fe}\right) - 0.827 * \ln\left(\frac{Co}{Fe}\right) - 0.306 * \ln\left(\frac{Ni}{Fe}\right) - 12.15$$

$$F2 = 0.384 * \ln\left(\frac{Mg}{Fe}\right) + 0.091 * \ln\left(\frac{Al}{Fe}\right) + 1.169 * \ln\left(\frac{V}{Fe}\right) - 0.75 * \ln\left(\frac{Mn}{Fe}\right) - 0.525 * \ln\left(\frac{Co}{Fe}\right) - 1.149 * \ln\left(\frac{Ni}{Fe}\right) - 11.256$$

For LDA2:

$$F1 = 0.627 * \ln\left(\frac{Mg}{Fe}\right) - 1.5 * \ln\left(\frac{Al}{Fe}\right) + 0.259 * \ln\left(\frac{Ti}{Fe}\right) - 0.404 * \ln\left(\frac{V}{Fe}\right) + 0.212 * \ln\left(\frac{Mn}{Fe}\right) - 0.541 * \ln\left(\frac{Co}{Fe}\right) - 0.567 * \ln\left(\frac{Ni}{Fe}\right) - 14.699$$

$$F2 = 0.477 * \ln\left(\frac{Mg}{Fe}\right) + 0.281 * \ln\left(\frac{Al}{Fe}\right) - 0.192 * \ln\left(\frac{Ti}{Fe}\right) + 0.79 * \ln\left(\frac{V}{Fe}\right) - 0.439 * \ln\left(\frac{Mn}{Fe}\right) + 0.215 * \ln\left(\frac{Co}{Fe}\right) - 1.043 * \ln\left(\frac{Ni}{Fe}\right) - 2.355$$

where F1 is Factor 1, F2 is Factor 2, and elements are in ppm.

Pisiak et al. (2017), and Morris et al. (2025).

Each re-analyzed bulk till sample (approximately 50 magnetite grains from each till sample) was 'scored' for its percentage of hydrothermal magnetite, ore igneous magnetite, or barren igneous magnetite using the LDA1 and LDA2 models of Pisiak et al. (2017). Discriminant functions vary between LDA models (see Pisiak et al., 2017), but element lists are similar (Mg, Al, V, Mn, Co, Ni, ±Ti; all normalized to Fe). Most noteworthy is that their LDA2 model, which includes Ti, is better than LDA1, where hydrothermal scoring results between the various methods from this study are within 6% of one another and within 4% of Pisiak et al. (2017) (Table 2).

4.2.1. Sample 12-PMA-094-A01

Using the LDA1 model from Pisiak et al., 2017, we score 16-18% hydrothermal magnetite grains for sample 12-PMA-094-A01, depending on method used (Table 2). In comparison, Pisiak et al. (2017) scored 22% hydrothermal magnetite grains for this sample using LDA1 (Table 2). Two magnetite grains identified by Pisiak et al. (2017) as hydrothermal (A16, B6, Morris et al., 2025) were not classified as such in this study using the LDA1 model, regardless of method for data reduction and/or calibration. Using the LDA2 model, we consistently score 22% hydrothermal magnetite for sample 12-PMA-094-A01, regardless of data reduction or calibration technique, which is similar to 24% hydrothermal by Pisiak et al. (2017; Table 2, Fig. 3). Ten of the 12 magnetite grains (all but A13 and B6) identified as hydrothermal in Pisiak et al. (2017) were reproducible as hydrothermal in LDA2 scoring in this study, with one additional magnetite grain (B3; Morris et al., 2025). Results from Method 3, our most efficient method, are compared to those of Pisiak et al. (2017) for the LDA2 model in Figure 4a.

4.2.2. Sample 12-PMA-098-A01

Using the LDA1 model, we consistently score 24% hydrothermal magnetite grains for sample 12-PMA-098-A01, except for Method 2 which only scored 10% (Table 2). In comparison, Pisiak et al. (2017) scored 18% hydrothermal magnetite grains for sample 12-PMA-098-A01 using LDA1 (Table 2). All but one grain (A15), in addition to four more grains added from our analyses (A8, D15, E13, E5; Morris et al., 2025) of Pisiak et al. (2017) were classified as hydrothermal in this study (Method 1, 3 and 4; LDA1). Using the LDA2 model from Pisiak et al. (2017), we score 20-24% hydrothermal magnetite grains for sample 12-PMA-098-A01, similar to 24% hydrothermal by Pisiak et al. (2017; Table 2, Fig. 3). Results from Method 3 are compared to those of Pisiak et al. (2017) for the LDA2 model in Figure 4b.

4.2.3. Sample 12-PMA-101-A02

Using the LDA1 model, we score 24-26% (Method 1, 3, and 4) or 12% (Method 2) hydrothermal magnetite grains for sample 12-PMA-101-A02, compared to 16% from Pisiak et al. (2017; Table 2). All magnetite grains identified as

Table 2. Hydrothermal magnetite scoring using various methods and discriminant techniques.

			12-PMA-094-A01 (n = 49)	12-PMA-098-A01 (n = 50)	12-PMA-101-A02 (n = 50)
LDA1	Method 1	HTP magnetite: n (%)	8 (16%)	12 (24%)	13 (26%)
	Method 2	HTP magnetite: n (%)	8 (16%)	5 (10%)	6 (12%)
	Method 3	HTP magnetite: n (%)	9 (18%)	12 (24%)	12 (24%)
	Method 4	HTP magnetite: n (%)	9 (18%)	12 (24%)	12 (24%)
	Pisiak et al. (2017)	HTP magnetite: n (%)	11 (22%)	9 (18%)	8 (16%)
LDA2	Method 1	HTP magnetite: n (%)	11 (22%)	12 (24%)	15 (30%)
	Method 2	HTP magnetite: n (%)	11 (22%)	10 (20%)	12 (24%)
	Method 3	HTP magnetite: n (%)	11 (22%)	11 (22%)	14 (28%)
	Method 4	HTP magnetite: n (%)	11 (22%)	11 (22%)	15 (30%)
	Pisiak et al. (2017)	HTP magnetite: n (%)	12 (24%)	12 (24%)	13 (26%)
Ti vs. Ni/Cr	Method 1	HTP magnetite: n (%)	3 (6%)	4 (8%)	9 (18%)
	Method 2	HTP magnetite: n (%)	3 (6%)	4 (8%)	9 (18%)
	Method 3	HTP magnetite: n (%)	2 (4%)	5 (10%)	9 (18%)
	Method 4	HTP magnetite: n (%)	3 (6%)	3 (6%)	9 (18%)

HTP refers to hydrothermal magnetite. See text for method descriptions. Ti versus Ni/Cr discrimination is from Dare et al. (2014). n = number of magnetite grains that scored as hydrothermal.

hydrothermal by Pisiak et al. (2017) using the LDA1 model were also identified as hydrothermal in this study (Methods 1, 3, 4) as were additional grains, depending on method (A5, A14, G4 ±A3, B4; Morris et al., 2025). Using the LDA2 model, we score 24-30% hydrothermal magnetite for sample 12-PMA-101-A02, similar to 26% hydrothermal by Pisiak et al. (2017; Table 2, Fig. 3). All of the magnetite identified by Pisiak et al. (2017) as hydrothermal using the LDA2 model was also identified as hydrothermal in this study (Methods 1, 3, and 4). Results from Method 3 are compared to those of Pisiak et al. (2017) for the LDA2 model in Figure 4c.

4.3. Hydrothermal scoring using Ti versus Ni/Cr

In addition to linear discriminant analyses models, we determined the scoring of hydrothermal magnetite from each till sample in Ti versus Ni/Cr space, a widely used diagram proposed by Dare et al. (2014) that broadly discriminates hydrothermal from igneous magnetite (Table 2, Fig. 5).

Discrimination in Ti versus Ni/Cr space for sample 12-PMA-094-A01 only scored 4-6% hydrothermal magnetite from this study, far lower than the 22% obtained from the LDA2 model (Table 2). Only one magnetite grain (B8) that scored as hydrothermal from the LDA2 model (Method 3) also scored as hydrothermal in Ti versus Ni/Cr space (Fig. 5a), indicating <10% of magnetite grains were reproducible in scoring as hydrothermal magnetite between LDA2 (Pisiak et al., 2017) and Ti vs. Ni/Cr (Dare et al., 2014) discrimination.

For sample 12-PMA-098-A01, discrimination in Ti versus Ni/Cr space only scored 6-10% hydrothermal magnetite, again far lower than the 20-24% obtained from the LDA2 model (Table 2). In addition, only two magnetite grains (F10, E13) that scored as hydrothermal from LDA2 (Method 3) also scored as hydrothermal in Ti versus Ni/Cr space (Fig. 5b), indicating <20% of magnetite grains were reproducible in scoring as hydrothermal magnetite.

Discrimination in Ti versus Ni/Cr space for sample 12-PMA-

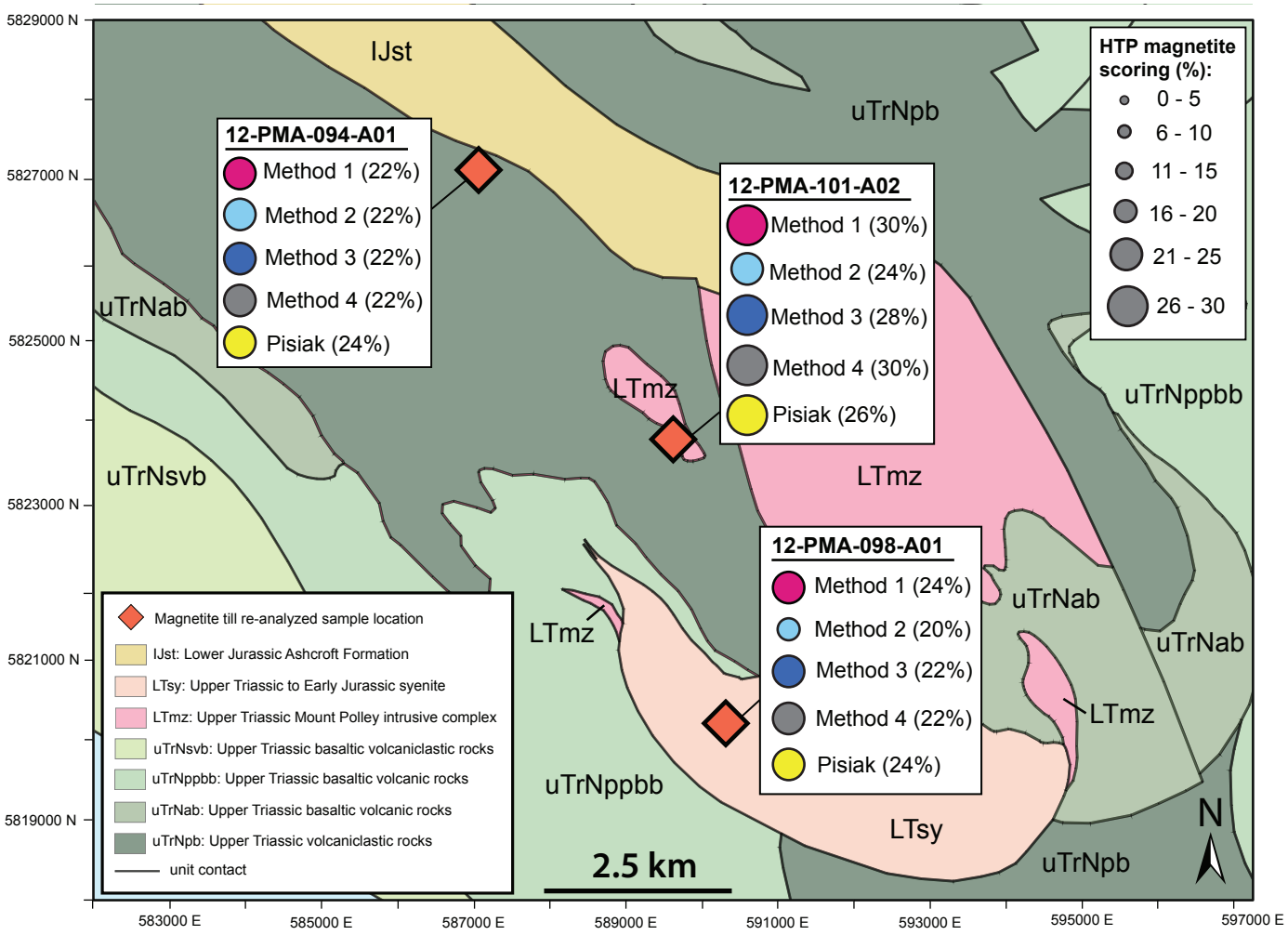

Fig. 3. Percentage of hydrothermal (HTP) magnetite scoring from revised methods (Methods 1 through 4) in this study compared to Pisiak et al. (2017) using the linear discriminant analyses 2 (LDA2) model of Pisiak et al. (2017). Magnetite analyzed is from bulk subglacial till samples collected close to the Mount Polley deposit. Bedrock geology is from Logan et al. (2010) and Cui et al. (2019). For contour elevations, water bodies, fault lines, and pit outlines see Figure 2.

101-A02 scored 18% hydrothermal magnetite from this study, lower than the 24-30% obtained from the LDA2 model (Table 2). Only four magnetite grains (A14, B7, C7, F9) that scored as hydrothermal from LDA2 (Method 3) scored as hydrothermal in Ti versus Ni/Cr space (Fig. 5c), indicating <40% of the magnetite grains were reproducible in scoring as hydrothermal magnetite.

5. Discussion

Our results demonstrate that reduced ablation dwell times by a factor of four (10 seconds, Method 3) with increased spot size (100 µm) and no editing of time-resolved spectra for inclusions, provides nearly identical scoring of hydrothermal magnetite to the more lengthy analytical Methods 1, 2, and 4. For example, Methods 1 and 2 employed data reduction techniques which would require considerable time (~4 hours per till sample with 50 grains analyzed) of plotting and sorting through time-resolved LA-ICP-MS spectra to find and edit inclusions encountered during magnetite ablation (e.g., apatite, sulphides). Of the ~150 magnetite grains analyzed, most are considered relatively inclusion free (<1 wt.% P and <0.3 wt.% S), except for grain D10 in sample 12-PMA-094-A01 (Method 4) and grain D8 in 12-PMA-098-A01 (Method 3 and 4), neither of which scored as hydrothermal magnetite regardless of method (Morris et al., 2025). The nearly identical scoring (i.e., within 6% for LDA2) of hydrothermal magnetite in till samples from only 10 seconds of ablation time per grain with no editing of time-resolved spectra (Method 3) compared to others in this study and Pisiak et al. (2017; Table 2) show promise to expedite analysis of magnetite in till samples, and efficiently score it for % hydrothermal grains. Although not all hydrothermal magnetite is related to mineralization (e.g., hydrothermal magnetite in barren plutons), the identification of only igneous magnetite in till would suggest a till sample that is not prospective. In addition, laser ablation systems that can run in automation mode, where the user can pre-select ablation

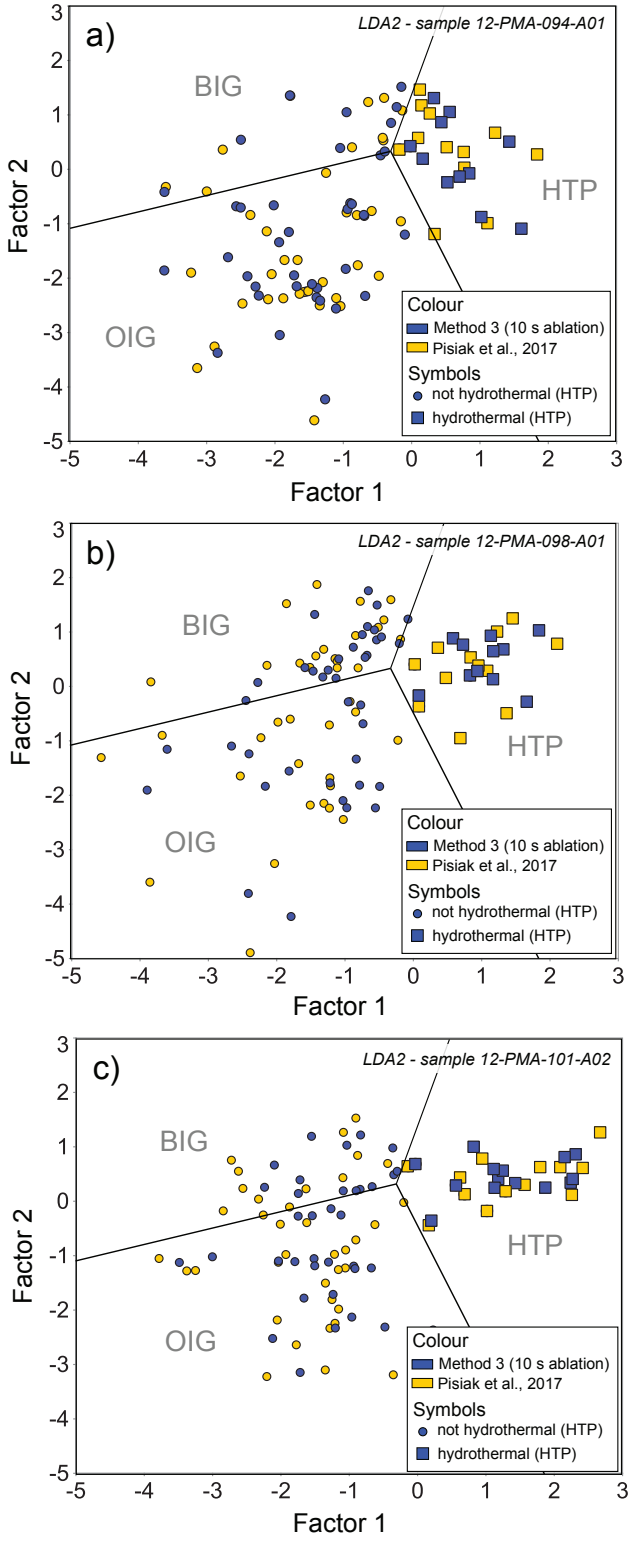

Fig. 4. Scoring of barren igneous magnetite (BIG), ore igneous magnetite (OIG), and hydrothermal magnetite (HTP) by applying the linear discriminant analysis model 2 (LDA2) of Pisiak et al. (2017). Scoring results from our most efficient workflow (Method 3) are shown with those from Pisiak et al. (2017) for samples **a)** 12-PMA-094-A01, **b)** 12-PMA-098-A01, and **c)** 12-PMA-101-A02. For factor 1 and 2 equations and boundaries between compositions groups see Pisiak (2015) and Morris et al. (2025).

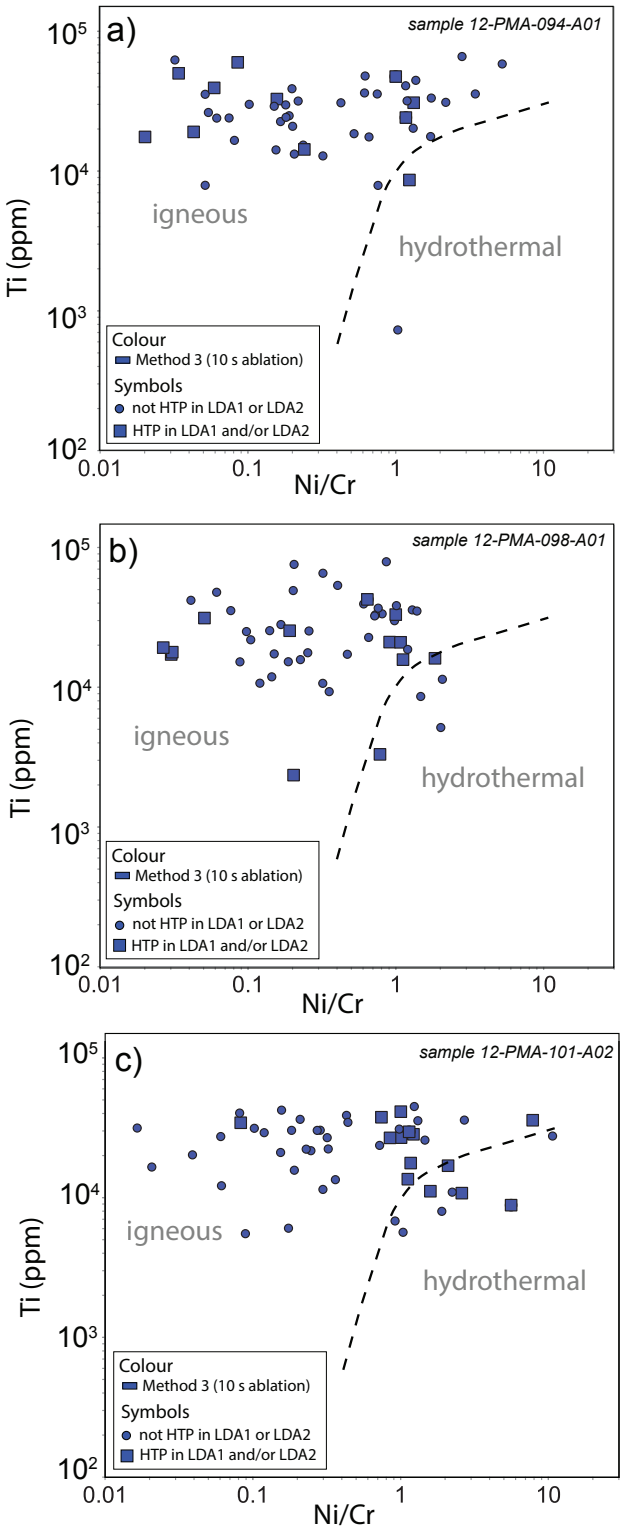

Fig. 5. Scoring of igneous versus hydrothermal magnetite based on Ti versus Ni/Cr (Dare et al., 2014) using analytical results from Method 3 (this study) for samples: **a)** 12-PMA-094-A01, **b)** 12-PMA-098-A01, and **c)** 12-PMA-101-A02. Blue squares indicate if magnetite scored as hydrothermal (HTP) using either LDA models of Pisiak et al. (2017).

spots and run analyses unsupervised, is suggested to further optimize workflow. Using sum normalization techniques (Liu et al., 2008) also forgoes the use of electron microprobe analysis before laser ablation, again saving user time in processing and scoring a till or stream-sediment sample for hydrothermal magnetite. Comparison of sum normalization values with those obtained using an internal standard shows values are within 3% (Morris et al., 2025), indicating sum normalization provides nearly identical results.

The largest differences in scoring of hydrothermal magnetite in subglacial till samples is from Method 2, which uses only NIST glass standards (NIST 611, 613) for calibration. For example, results from sample 12-PMA-098-A01 and 12-PMA-101-A02 scored nearly half the amount hydrothermal magnetite in LDA1 models using Method 2, in comparison to other methods. Greater relative % differences (>10%) from known versus measured values in external standards (BHVO-2g and BCR-2g) for elements such as: Fe, Cu, Zn, ±Co, Mn, Ni, and V suggests NIST glass standards, such as NIST 611 and 613, are not ideal calibrants for magnetite analyses. For example, relative per cent differences between known and measured values from BHVO-2g and BCR-2g for Method 2 measured lower Fe values for samples 12-PMA-098-A01 and 12-PMA-101-A02 (Fe relative % difference is -13 to -18%, Table 1). Lower Fe contents for magnetite determined by Method 2 in samples 12-PMA-098-A01 and 12-PMA-101-A02 likely resulted in the underscoring of the % hydrothermal magnetite in these samples for LDA1 and LDA2 analyses (Table 2). Because the transition from igneous to hydrothermal magnetite is essentially a 'progressive chemical purification' towards pure Fe_3O_4 with increasing Fe content (Wen et al., 2017), properly calibrating and analyzing for Fe is important for identifying hydrothermal magnetite using LA-ICP-MS techniques. From this study, we show that calibration techniques that include basaltic glass standards (i.e., BHVO-2g), which have higher Fe content (11.2-12.8 wt.%) is better than only using NIST glass standards (i.e., NIST 611 and 613) with lower Fe content (<500 ppm), because the former is closer to magnetite Fe contents (up to ~72 wt.%).

Reproducibility in identifying hydrothermal magnetite is most similar for discriminant analyses using the LDA2 model, in which results from our study were within 4% of scoring from Pisiak et al. (2017; Table 2). This is likely due to the inclusion of Ti, in the LDA2 model. Future work could test reproducibility of scoring with other discriminant models that include Ga and Ge (Sievwright, 2018; McCurdy et al., 2022) but with a reduced element list. Such a list would remove elements that identify inclusions (i.e., Na, Si, P, S, K, Ca, and Ba) and, using an optimized workflow similar to our Method 3, would negate the need for data reduction around minor inclusions considering the magnetite is relatively inclusion free.

Plotting the results of our study in Ti versus Ni/Cr space to distinguish hydrothermal from igneous magnetite (Dare et al., 2014), shows poor reproducibility in identifying hydrothermal magnetite (<40%) compared to results from our LDA analyses. For example, only one grain that scored as hydrothermal magnetite from sample 12-PMA-094-A01 also scored as hydrothermal in Ti versus Ni/Cr space (Fig. 5a). We therefore suggest that, although the Ti versus Ni/Cr plot is rapid and simple, it is an ineffective discriminant for identifying hydrothermal magnetite collected in subglacial till.

6. Summary

An LA-ICP-MS protocol using 10 sec laser ablation dwell times and 100 μm ablation spot sizes scores nearly identical percentages of hydrothermal magnetite in subglacial till samples compared to the typical more time-consuming analytical methods (editing time-resolved spectra around inclusions, longer dwell times). Application of our Method 3 reduces the time in identifying hydrothermal magnetite in till samples, making for a more rapid and efficient approach in an exploration program. Including basaltic glass standards in calibration techniques is preferred over only using NIST glass standards, which have Fe contents far below (ppm concentrations) that of magnetite (up to 72 wt.% Fe). Reproducibility of hydrothermal magnetite from linear discriminant analysis models of Pisiak et al. (2017) indicates LDA2, which includes Ti, is better than LDA1, where scoring reproducibility is within 6%, regardless of the method employed. Reproducibility of hydrothermal magnetite in Ti versus Ni/Cr space is poor (<40%).

Acknowledgments

We thank Wyatt Bain (BCGS) and Evan Orovan (BCGS) for discussions that motivated much of this work and Travis Ferbey (BCGS), Jim Logan (BCGS retired), and Alexei Rukhlov (BCGS), for thorough reviews and comments. Till collection and sample processing were supported by Natural Resources of Canada Targeted Geoscience Initiative 4 grants to Alain Plouffe (GSC Ottawa) and Travis Ferbey (BCGS); we are grateful to them for access to till samples. This research was supported by a British Columbia Ministry of Mining and Critical Minerals-University of Victoria Partnership Project Grant and a NSERC Discovery Grant 154275 (Canil).

References cited

Canil, D., Grondahl, C., Lacourse, T., and Pisiak, K.L., 2016. Trace elements in magnetite from porphyry Cu-Mo-Au deposits in British Columbia. Ore Geology Reviews, 72, 1116-1128. <https://doi.org/10.1016/j.oregeorev.2015.10.007>

Clarke, G., Northcote, B.K., Corcoran, N.L., Pothorin, C., Heidarian, H., and Hancock, K., 2024. Exploration and Mining in British Columbia, 2023: A summary. In: Provincial Overview of Exploration and Mining in British Columbia, 2023. British Columbia Ministry of Energy, Mines and Low Carbon Innovation, British Columbia Geological Survey Information Circular 2024-01, pp. 1-53.

Colpron, M., 2020. Yukon terranes-A digital atlas of terranes for the northern Cordillera. Yukon Geological Survey. <https://data.geology.gov.yk.ca/Compilation/2#InfoTab>

Cui, Y., Miller, D., Schiarizza, P., and Diakow, L.J., 2017. British Columbia digital geology. British Columbia Ministry of Energy, Mines, and Petroleum Resources, British Columbia Geological Survey Open File 2017-8, 9 p. Data version 2019-12-19.

Dupuis, C., and Beaudoin, G., 2011. Discriminant diagrams for iron oxide trace element fingerprinting of mineral deposit types. Mineralium Deposita, 46, 319-335. <https://doi.org/10.1007/s00126-011-0334-y>

Haggerty, S.E., 1976. Opaque mineral oxides in terrestrial igneous rocks. In: Rumble, D., (Ed.), Reviews in Mineralogy, Volume 3: Oxide Minerals, pp. Hg-101-Hg-300.

Haggerty, S.E., 1991. Oxide textures-A Mini-Atlas. In: Ribbe, P.H., (Ed.), Reviews in Mineralogy, Volume 25, Oxide Minerals: Petrologic and Magnetic Significance, pp. 129-137. <https://doi.org/10.1515/9781501508684-008>

Hashmi, S., Ward, B.C., Plouffe, A., Leybourne, M.I., and Ferbey, T., 2015. Geochemical and mineralogical dispersal in till from the Mount Polley Cu-Au porphyry deposit, central British Columbia, Canada. Geochemistry: Exploration, Environment, Analysis, 15, 234-249. <https://doi.org/10.1144/geochem2014-310>

Huang, X.W., Sappin, A.A., Boutroy, E., Beaudoin, G., and Makvandi S., 2019. Trace element composition of igneous and hydrothermal magnetite from porphyry deposits: Relationship to deposit subtypes and magmatic affinity. Economic Geology, 114, 917-952. <https://doi.org/10.5382/econgeo.4648>

Jochum, K.P., Willbold, M., Raczek, I., Stoll, B., and Herwig, K., 2005. Chemical characterization of the USGS reference glasses GSA-1G, GSC-1G, GSE-1G, BCR-2G, BHVO-2G, and BIR-1G using EMPA, ID-TIMS, ID-ICP-MS, and LA-ICP-MS. Geostandards and Geoanalytical Research, 29, 285-302. <https://doi.org/10.1111/j.1751-908X.2005.tb00901.x>

Jochum, K.P., Weis, U., Stoll, B., Kuzmin, D., Yang, Q., Raczek, I., Jacob, D.E., Stracke, A., Birbaum, K., Frick, D.A., Günther, D., and Enzweiler, J., 2011. Determination of reference values for NIST SRM 610-617 glasses following ISO guidelines. Geostandards and Geoanalytical Research, 35, 397-429. <https://doi.org/10.1111/j.1751-908X.2011.00120.x>

Liu, Y., Hu, Z., Gao, S., Günther, D., Xu, J., Gao, C., and Chen, H., 2008. In situ analysis of major and trace elements of anhydrous minerals by LA-ICP-MS without applying an internal standard. Chemical Geology, 257, 34-43. <https://doi.org/10.1016/j.chemgeo.2008.08.004>

Logan, J.M., and Mihalynuk, M., 2005. Regional geology and setting of the Cariboo, Bell, Springer, and Northeast porphyry Cu-Au zones at Mount Polley, South-Central British Columbia. In: Geological Fieldwork 2004, British Columbia Ministry of Energy, Mines and Petroleum Resources, British Columbia Geological Survey Paper 2005-1, pp. 249-270.

Logan, J.M., Mihalynuk, M.G., Ullrich, T., and Friedman, R.M., 2007. U-Pb ages of intrusive rocks and $^{40}Ar/^{39}Ar$ plateau ages of copper-gold-silver mineralization associated with alkaline intrusive centres at Mount Polley and the Iron Mask Batholith, Southern and Central British Columbia. In: Geological Fieldwork 2006, British Columbia Ministry of Energy, Mines and Petroleum Resources, British Columbia Geological Survey Paper 2007-1, pp. 93-116.

Logan, J.M., Schiarizza, P., Struik, L.C., Barnett, C., Nelson, J.L., Kowalczyk, P., Ferri, F., Mihalynuk, M.G., Thomas, M.D., Gammon, P., Lett, R., Jackaman, W., and Ferbey, T., 2010. Bedrock Geology of the QUEST map area, central British Columbia. British Columbia Geological Survey Geoscience Map 2010-1, Geoscience BC Report 2010-5 and Geological Survey of Canada, Open File 6476.

McCurdy, M.W., Peter, J.M., McClenaghan, M.B., Gadd, M.G., Layton-Matthews, D., Leybourne, M.I., Garrett, R.G., Petts, D.C., Jackson, S.E., and Casselman, S., 2022. Evaluation of magnetite as an indicator mineral for porphyry Cu exploration: a case study using bedrock and stream sediments at the Casino porphyry Cu-Au-Mo deposit, Yukon, Canada. Geochemistry: Exploration, Environment, Analysis, 22, 1-22. <https://doi.org/10.1144/geochem2021-072>

Morris, R., Canil, D., and Lacourse, T., 2025. LA-ICP-MS data files for optimized workflow analyses and reproducibility of hydrothermal magnetite as an indicator for porphyry copper deposits. British Columbia Ministry of Mining and Critical Minerals, British Columbia Geological Survey GeoFile 2025-10, 1 p.

Nadoll, P., Angerer, T., Mauk, J.L., French, D., and Walshe, J., 2014. The chemistry of hydrothermal magnetite: A review. Ore Geology Reviews, 61, 1-32. <https://doi.org/10.1016/j.oregeorev.2013.12.013>

Nadoll, P., Mauk, J.L., Leveille, R.A., and Koenig, A.E., 2015. Geochemistry of magnetite from porphyry Cu and skarn deposits in the southwestern United States. Mineralium Deposita, 50, 493-515. <https://doi.org/10.1007/s00126-014-0539-y>

NRCan, 2022. The Canadian critical minerals strategy. Natural Resources Canada, 52 p. <https://www.canada.ca/en/campaign/critical-minerals-in-canada/canadian-critical-minerals-strategy.html>

Paton, C., Hellstrom, J., Paul, B., Woodhead, J., and Hergt, J., 2011. Iolite: Freeware for the visualisation and processing of mass spectrometric data. Journal of Analytical Atomic Spectrometry. <https://doi.org/10.1039/C1JA10172B>

Paul, B., Petrus, J.A., Savard, D., Woodhead, J., Hergt, J., Greig, A., Paton, C., and Raynor, P., 2023. Time resolved trace element calibration strategies for LA-ICP-MS. Journal of Analytical Atomic Spectrometry. <https://doi.org/10.1039/D3JA00037K>

Pisiak, L.K., 2015. Magnetite as a porphyry Cu indicator mineral: A test using the Mount Polley porphyry Cu-Au deposit south-central British Columbia. Unpublished M.Sc. thesis, University of Victoria, Victoria, Canada, 149 p. <http://hdl.handle.net/1828/6992>

Pisiak, L.K., Canil, D., Lacourse, T., Plouffe, A., and Ferbey, T., 2017. Magnetite as an indicator mineral in the exploration of porphyry deposits: A case study in till near the Mount Polley Cu-Au deposit, British Columbia, Canada. Society of Economic Geologist, 112, 919-940. <https://doi.org/10.2113/econgeo.112.4.919>

Plouffe, A., and Ferbey, T., 2016. Till geochemistry, mineralogy, and textural data near four Cu porphyry deposits in British Columbia. Geological Survey of Canada, Open File 8038, British Columbia Ministry of Energy and Mines, British Columbia Geological Survey GeoFile 2016-10, 44 p.

Rees, C., Gillstrom, G., Ferreira, L., Bjornson, L., and Taylor, C., 2014. Geology of the Mount Polley intrusive complex, Geoscience BC Map 2014-08-1, 1:10,000 scale.

Ryder, J.M., Fulton, R.J., and Clague, J.J., 1991. The Cordilleran Ice Sheet and the glacial geomorphology of southern and central British Columbia. Géographie Physique et Quaternaire, 45, 365-377. <https://doi.org/10.7202/032882ar>

Sievwright, R.H., 2018. Developing magnetite chemistry as an exploration tool for porphyry copper deposits, Unpublished PhD dissertation, Department of Earth Science and Engineering Imperial College London, 344 p.

Wen, G., Li, J-W., Hofstra, A.H., Koenig, A.E., Lowers, H.A., and Adams, D., 2017. Hydrothermal reequilibration of igneous magnetite in altered granitic plutons and its implications for magnetite classification schemes: Insights from the Handan-Xingtai iron district, North China Craton. Geochimica et Cosmochimica Acta, 213, 255-270. <https://doi.org/10.1016/j.gca.2017.06.043>

Xiao, X., Zhou, T-f., White, N.C., Fan, Y., Zhang, L-j., and Chen, X-f., 2023. Systematic textural and geochemical variations in magnetite from a porphyry-skarn Cu (Au) system and implications for ore formation, perspective from Xinqiao Cu-Fe-Ah deposit, eastern China. Ore Geology Reviews, 153, article 105271. <https://doi.org/10.1016/j.oregeorev.2022.105271>